Research article

Effect of a bioinspired upstream extended surface profile on flow characteristics and a drag coefficient of a circular cylinder

Shorob Alam Bhuiyan, Ikram Hossain, Redwan Hossain, Md. Sakib Ibn Mobarak Abir and Dewan Hasan Ahmed*

Department of Mechanical and Production Engineering, Ahsanullah University of Science and Technology, 141-142 Love Road, Tejgaon Industrial Area, Dhaka-1208, Bangladesh

* **Correspondence:** dhahmed.mpe@aust.edu; Tel: 880-2-8870422; Fax: 880-2-8870417-18.

Abstract: In the current work, the passive drag reduction of a circular cylinder for the subcritical Reynolds number range of 5.67×10^4 to 1.79×10^5 was computationally and experimentally investigated. First, inspired by nature, the aerodynamic drag coefficient of a whole Peregrine Falcon was measured in a subsonic wind tunnel for various angles of attack and Reynolds numbers (Re) and compared with the bare cylinder. At a 20° angle of attack and $Re = 5.67 \times 10^4$, the whole falcon model had a 75% lower drag coefficient than the bare cylinder. Later, with the moderate Falcon model, in which the falcon's beak and neck were linked to the cylinder as an extended surface, the drag coefficient decreased up to 72% in the subcritical Reynolds number zone. Finally, the extended surface with a falcon beak profile was connected to the cylinder with a stem and investigated both numerically and experimentally for various stem lengths, angles of attack, and Reynolds numbers. It was found that at low Re, the drag coefficient can be reduced by up to 47% for the stem length of 80 mm ($L/D = 1.20$) with an angle of attack 10°. The computational investigation yielded precise flow characteristics, and it was discovered that the stem length and the Re had a substantial influence on vortex generation and turbulent kinetic energy between the beak and cylinder, as well as downstream of the cylinder. Investigation revealed that percentile drag reduction was much lower for the whole Falcon model over a wide range of Reynolds numbers and positive angles of attack, which exist in nature. Similarly, when compared to the other stem lengths, the 60 mm stem length ($L/D = 0.97$) produced similar results to the whole Falcon model. The numerical results were well validated with the experimental results.

Keywords: bio-inspired; drag reduction; peregrine falcon; extended surface; subcritical Reynolds numbers

1. Introduction

In the realm of fluid dynamics, the investigation of fluid flow around bluff bodies, exemplified by circular cylinders, holds vital significance for numerous engineering applications such as in heat exchangers, cooling towers, nuclear cooling systems, and submarine pipelines [1]. While a multitude of studies have explored drag reduction strategies, the uniqueness of this research lies in its commitment to advancing the understanding of fluid dynamics and offering innovative solutions. The drag coefficient for a circular cylinder works transversely as a function of the Reynolds number, as stated by Schlichting and Gersten [2]. As the Reynolds number rises, the drag coefficient tends to decline to a certain point; then, there is an inevitable fall in the drag coefficient at the critical Reynolds regime ($Re = 4 \times 10^5$).

Drag affects fuel consumption in various applications; hence several studies have identified active and passive drag-reduction solutions as effective. Eun et al. [3] found that a bluff body with boat and hump tails reduced drag by 50.9% due to a significant pressure drop before and after the boat tail. Frolov and Kozlova [4] and García-Baena et al. [5] passively reduced drag on a bluff body utilizing flat and rear plates. Flat plates parallel to the fluid flow direction reduced drag by 30%, while rear plates enhanced plate flexibility and reduced drag. Placing in corresponding places, an upstream circular cylinder will lessen the drag of a downstream circular cylinder. Igarashi [6] and Zdravkovich [7] categorized the wake flow of such tandem arrangements as extended body regime, reattachment zone, and co-shedding zone. Xu and Zhou [8] further subdivided the reattachment into two sub-regimes, with one occurring upstream of the downstream cylinder and the other downstream. Wu et al. [9], Lin et al. [10], and Carmo et al. [11] examined the wake structures of circular cylinders in tandem and classified various flow configurations based on the distance between the upstream and downstream cylinders.

Rather than a comparable cylinder, a small control rod put upstream in tandem configuration greatly reduces total drag. The drag coefficient was only 0.42 times that of the single cylinder after inserting the tiny rod upstream at a Reynolds number of 6.5×10^4 [12]. Furthermore, if the distance between the rod and the downstream cylinder remains fixed, the drag is proportional to the rod's size [13,14]. Drag increases at $Re = 0.8 \times 10^4$ to 2.42×10^4 when rod size or distance between the rod and downstream cylinder decreases [15]. Modifying the shape of the upstream bluff body was also found to have positive effects by several researchers. Prasad and Williamson [16] positioned a flat plate perpendicular to the flow and 1.5 diameters upstream of the test cylinder to minimize drag by 38 percent. Moreover, modifying the upstream bluff body to a T-shaped plate, C-shaped, or equilateral triangular wedge had a comparable beneficial effect on reducing drag [17–19].

For infinite bluff bodies, surface modification techniques such as roughness and dimples, helical wire, vortex generators, and grooved and patterned surfaces were proposed as effective drag-reduction strategies [20–24]. In the instance of a finite cylinder, Haidary et al. [25] examined how the addition of a channel through a circular cylinder at several longitudinal positions and angles lowered drag. At high Reynolds numbers, various orientations of flow through a cylinder decrease drag by 31%. Asif et al. [26] investigated bird flapping to reduce drag and found that small flaps reduce drag by 73%, whereas continuous flaps reduce drag by 66%. Furthermore, the utilization of a carefully designed membrane, inspired by the wing structure of bats, has the potential to enhance both the average lift and efficiency [27,28]. To determine the impact of an extended upstream surface on the overall drag of finite circular cylinders in a turbulent flow, Shoshe et al. [29] experimentally investigated five different

cylinder diameters and five different stem lengths, indicating that extended surfaces with finite cylinders placed at specific distances could effectively reduce pressure-induced drag to a maximum of 60%. Furthermore, changing the shape of the extended surface to a C-shape and placing it at an upstream distance of 66 % (i.e. $L/D = 0.66$) of the main cylinder reduces drag by about 55% [30].

Numerous studies have attempted to reduce drag using various bio-inspired ways, with shark riblets being the most prominent as it delays boundary layer separation, resulting in a 7.59% reduction in drag [31]. Siddiqui and Agelin-Chaab [32] did a review paper on fishes (Nekton), birds (avian), and fast-running land animals as a source of inspiration for drag reduction; each of these species has unique characteristics. However, the ability of birds to glide and alter the shape of their wings and tails to control the trajectory and velocity of their flight makes them more suitable for a bio-inspired model than other species [33–35]. The Peregrine Falcon is the fastest bird, reaching speeds of up to 150 km/h; thus, numerous researchers, like Selim et al. [36] and Ponitz et al. [37], have researched it. It was discovered that Peregrine Falcons adopt M-shaped flying configurations throughout the pullout maneuver and forward sweep main feathers to provide the high lift required at the end of the pullout while keeping the angle of incidence as low as possible to reduce drag. Therefore, by specifically focusing on the flow characteristics and drag coefficient of a circular cylinder with an irregular profile inspired by a Falcon's beak-like extended surface, this study aims to introduce a novel dimension to drag reduction methodologies.

CFD modeling is popular and economical today for gaining a better knowledge of the differences in coefficients of drag and determining solutions to reduce drag. In addition, many studies compare 2D- dimensional and 3D- dimensional simulations [38,39] as well as two distant solvers such as ANSYS CFX 13.0 and OpenFOAM [40] to find the best numerical method that requires less computational time and is accurate with experimentation. Two-dimensional modeling has justified findings in some instances, such as predicting the shape changes of droplets during freefall [41] but not in turbulent conditions.

Therefore, despite the existing body of research on drag reduction, the need for continued investigation remains imperative. Industries are increasingly seeking more efficient and sustainable solutions, prompting researchers to explore unconventional avenues. In this context, the current study stands out by addressing a critical gap in the literature—examining the effectiveness of an irregular profile inspired by a Falcon's beak-like extended surface. In a field saturated with conventional methods, this research represents a fresh and potentially groundbreaking approach that could redefine the understanding of passive drag reduction strategies for circular cylinders.

By specifically considering different upstream positions and angles of attack for the extended surface, the study adds nuance to the exploration, aiming to unravel how variations in these parameters impact drag reduction. Thus, the research not only contributes to the broader knowledge of fluid dynamics but also offers a unique perspective that has the potential to significantly enhance the efficiency and sustainability of engineering applications. In summary, the current study is not merely an addition to the existing literature; it represents a crucial step toward innovation in drag reduction methodologies, introducing an unconventional yet promising avenue for future engineering advancements.

1.1. Physical model

We are motivated by upstream extended surface and bio-inspired drag reduction techniques. The research included a bio-inspired form, namely the beak of the Peregrine Falcon, into the upstream

extended surface. Besides the 'SR-71' jet [42], there is a dearth of literature on that portion of the Peregrine Falcon; the goal of the study was to explore boundary layer separation and vortex production behind the extended surface and circular cylinder. Furthermore, the overall percentile of drag reduction of the bluff body. Using a streamlined object, such as the peregrine falcon's beak, as an extended surface of a cylinder can reduce drag by enhancing airflow around the cylinder. This is because the streamlined design of the beak serves to reduce turbulence and separation of the air traveling over the surface, which can result in drag. In this work, both experimental and numerical studies were conducted. The drag coefficient of the bare cylinder was initially calculated in a subsonic wind tunnel. On the designed extended surface based on the Peregrine Falcon, stem length was varied for various flow conditions in the subsequent trials. ANSYS 2021 R1 was used to do numerical simulation, wherein bare numerical simulation was performed on the cylinder with all validation and verification from the literature. Thirty-six simulations were then conducted with the extended surface in three distinct stem lengths (i.e., upstream places), which were 80 mm, 70 mm, and 60 mm. This simulation study was continued for different Reynolds numbers such as 5.67×10^4, 1.27×10^5 and 1.70×10^5. All the simulations were then compared with experiments done on the extended surface model. Later, another part of the experimentation was done on a moderate Falcon, where between the cylinder and extended surface, there will be upper and lower surfaces based on the shape of an actual Peregrine Falcon, and finally, a whole model of a Peregrine Falcon was designed to experiment in the wind tunnel. In the experimentation, various angles of attack were also observed and analyzed.

2. Experimental study

2.1. Extended surface peregrine falcon and fabrication

For the extended surface design of the chosen models, SOLIDWORKS 2020 R1 was used. For the dimensions of the model, necessary steps were taken, such as using Tracker analysis software. The whole Falcon body from the beak to the tail is measured at 380 mm by Johansson et al. [43], and the measured length was used as a reference to measure the rest of the necessary perimeters such as the beak and a circle diameter covering the middle portion of the Peregrine Falcon. Thus, Figure 1(a) illustrates the body shape measurement in which the circle in the middle has a diameter of about 85.05 mm, and the distance from the beak to the circle is approximately 78.64 mm. Therefore, the measured diameter and distance are utilized as the diameter for the circular cylinder and stem length displayed in Figure 1(b). For the numerical calculations, the diameter (D) and beak length were considered as 85 mm, and 22.3 mm, respectively. The stem lengths are varied with 60, 70, and 80 mm.

After carrying out all the necessary designs in SOLIDWORKS 2020 R1, the model is then fabricated by a 3D printer. The blockage ratio of the Peregrine Falcon model is 9.24% of the test section of the wind tunnel. Three different models were fabricated for carrying out the necessary experimental investigation. The first model is only considered the beak of the Falcon and considered as the cylinder with an extended surface, as shown in Figure 1(c). Later, the moderate Peregrine Falcon is an updated version of the extended surface where both the upper and lower surfaces is added between the beak and cylinder. As shown in Figure 1(d), both the upper and lower surface are designed according to the Peregrine Falcon head and neck shape. Finally, for a better understanding of the percentile of drag reduction, a whole Peregrine Falcon model is also designed and tested as shown in Figure 1(e) and (f). The model was designed based on real life with a scale ratio of 1:1.5 [43].
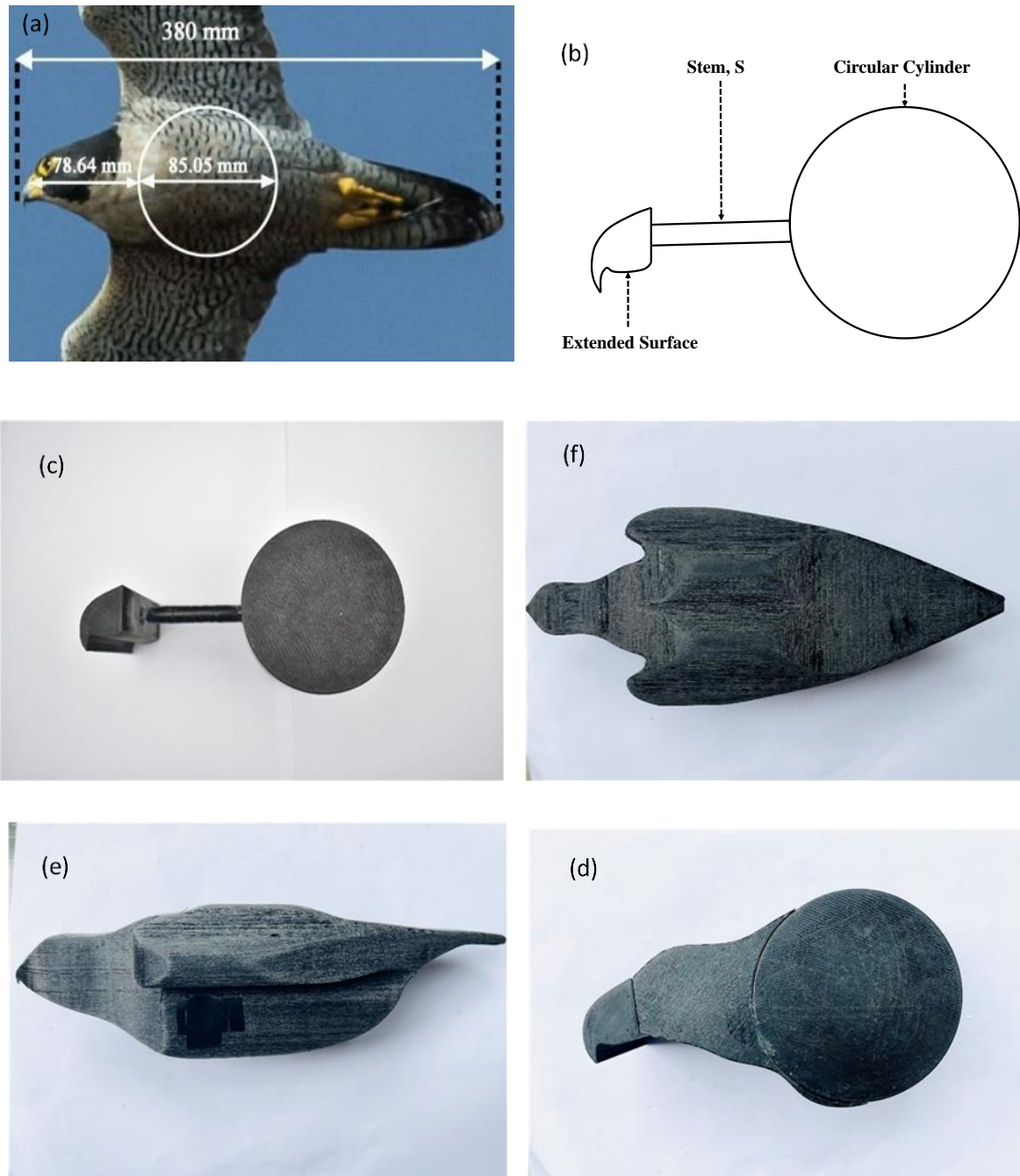
Figure 1. (a) Peregrine Falcon measurements, (b) Schematic diagram of the extended surface with a circular cylinder, Fabrication of Peregrine Falcon (c) extended surface model, (d) moderate Falcon model, (e) whole Falcon model side view, and (f) whole Falcon model top view.
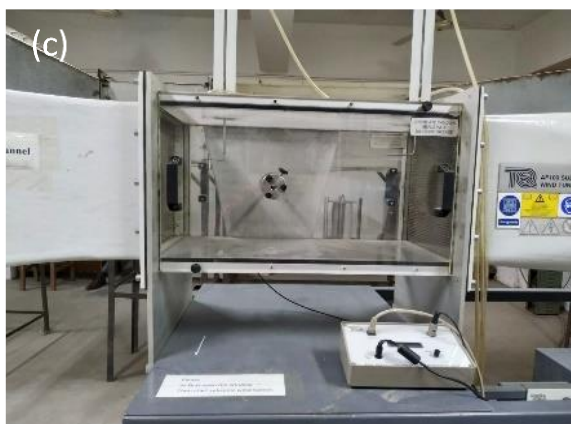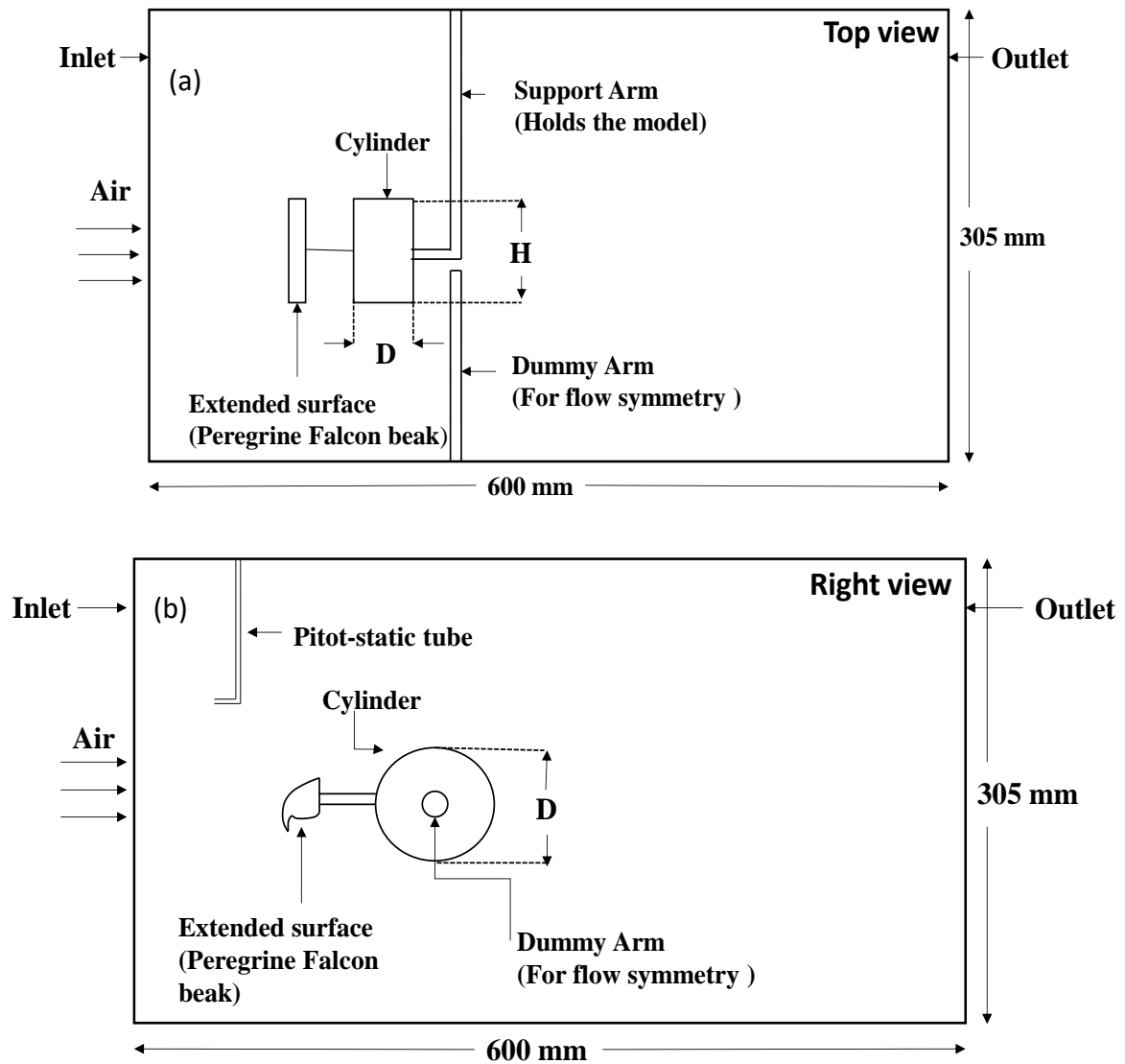
2.2. Test section

Figure 2. Schematic diagram of the test section with an extended surface model (a) top view, (b) right view, (c) AFA2-Balance Assembly, and (d) Digital display of AFA2 and DT-8920 digital manometer.

The experimentation was done in an AF100 subsonic wind tunnel from TecQuipment. Figure 2(a) and (b) show the schematic diagram of the experimental arrangement with the top and right-side view. All the necessary information on the wind tunnel and validity of the testing accuracy were carried out as per the literature such as Haidary et al. [25], Asif et al. [26], and Shoshe et al. [29]. The wind tunnel test section (as shown in Figure 2(c)) was 600 mm long with a cross-section of 305 mm × 305 mm with the operating range of air velocity was 0 to 36 m/s. The wind tunnel has a standard deviation of the mean velocity of less than 1%, and the RMS value is less than 0.03%. In the test section, a standard pitot-static tube along with a digital DT-8920 manometer (Figure 2(d)) was used to find the dynamic pressure readings having an accuracy of ± 0.3 % and ± 0.2% repeatability [29]. In Figure 2, D and H represent the cylinder's diameter and height, respectively.

2.3. Measurement of drag force

For measuring the drag force, AFA2- Balance Assembly was used. The dummy transmits the force felt on the model to the strain gauge load cell of the AFA2-Balance Assembly, and the readings can be seen instantaneously from its digital display. For symmetry, another dummy arm is set on the opposite side of the circular model. To get the required drag force from the model, at first, the force on the dummy arm (F_{arm}) is measured, then the force on the model along with the dummy arms ($F_{measured}$) is measured. By subtracting F_{arm} from the $F_{measured}$, the required drag force F_{bare} or $F_{modified}$ can be found, which denotes a bare cylinder without an extended surface and with the extended surface, respectively.

$$F_{\text{modified}} = F_{measured} - F_{arm} \tag{1}$$

$$F_{bare} = F_{measured} - F_{arm} \tag{2}$$

Then, the calculated drag force will be placed in the drag coefficient formula and compared.

$$C_{D_b} = \frac{2F_{bare}}{\rho U^2 A} \tag{3}$$

$$C_{D_b} = \frac{2F_{modified}}{\rho U^2 A} \tag{4}$$

Here, in Eqs. 3 and 4, 'A' denotes the reference area, which is the multiplication of height (H) and diameter (D).

2.4. Uncertainty analysis

For experimentation, uncertainty analysis is a must. For every model, uncertainty is done by calculating the standard deviation (SD), standard error (SE), and relative standard deviation (RSD) [44].

$$SD = \sqrt{\frac{\sum_1^N (X_i - X_n)^2}{N}} \tag{5}$$

$$SE = \frac{SD}{\sqrt{N}} \tag{6}$$

$$RSD = \frac{SD}{X_n} \tag{7}$$

Here,

$X_i = Value$

$X_n = Mean$

$N = Number\ of\ values$

For finding the standard deviation, various steps were taken for each model several ways drag force was collected. The drag force was changed by changing the pressure head in the wind tunnel. As the drag force fluctuates in the wind tunnel, at first, for each value, 2 minutes were observed, and for every 10 seconds, the values were recorded. Then again, without respect to time, the drag force was recorded both by increasing the pressure head and then again lowering the pressure head. After collecting several data for each value, standard deviation (*SD*), Standard error (*SE*), and relative standard deviation were calculated. The maximum standard error is 0.04, and the relative standard deviation is below 5%. For finding the uncertainty of the drag coefficient, uncertainties of the product function are used. Eq. 8 is,

$$\omega_R = \sqrt{\sum(\frac{\partial R}{\partial X_i} \times \omega_{X_i})^2} \tag{8}$$

where the ω_R represents the uncertainty of the result R and ω_{X_i} represents the uncertainty of the independent variable X_i. For the rest of the cases and models, the uncertainty is done in the same way. Details of the procedure can be found in [44].
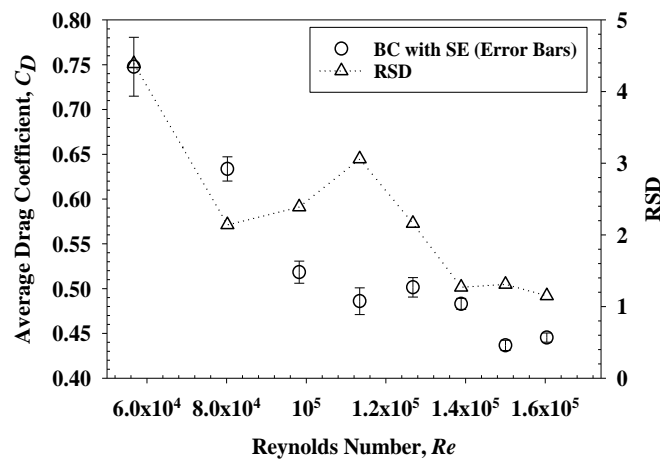

Figure 3. Average drag coefficient values with respective standard error (*SE*) and relative standard deviation (*RSD*) for bare cylinder (*BC*) in a range of Reynolds numbers.

Figure 3 displays the relative standard deviation (*RSD*) on the right y-axis and the average drag coefficient on the left y-axis. At a low Reynolds number, the *SD*, *SE*, and *RSD* were high and were 0.03, 0.03, and 4.4% for $Re = 5.67 \times 10^4$. As Reynolds' number increases, *RSD* decreases, and experiments are conducted at lower *RSD* ranges, indicating less uncertainty and raising the acceptability of the investigation conducted in this study.

3. Numerical study

3.1. Mathematical model

As a part of the comprehensive study on drag reduction at the subcritical Reynolds number region, numerical studies are carried out. Indeed, two-dimensional incompressible transient flow over a circular cylinder is considered for numerical studies. The continuity equation for the conservation of mass is:

$$\frac{\partial u}{\partial x} + \frac{\partial v}{\partial y} = 0 \tag{9}$$

where the fluid velocity inflow field is addressed by velocity components u and v and is in the general function of location (x, y). For conservation of momentum in a viscous flow, Navier-stokes equations are used:

$$\frac{\partial(\rho u)}{\partial t} + \nabla \cdot (\rho u \boldsymbol{V}) = -\frac{\partial p}{\partial x} + \rho f_x + (F_x)_{viscous} \tag{10}$$

$$\frac{\partial(\rho v)}{\partial t} + \nabla \cdot (\rho v \boldsymbol{V}) = -\frac{\partial p}{\partial y} + \rho f_y + (F_y)_{viscous} \tag{11}$$

where ρ denotes the density, $\boldsymbol{V}$ represents velocity vector field, (u, v) denotes velocity components, f, and F denote body force and viscous force, and p is the pressure [42].

For the numerical transition SST k-ω model was used. The transition SST model is used to model turbulent flows, where a significant proportion of the boundary layer is laminar. This model is also known as the γ-Re_θ model because it employs the γ and Re_θ equations as well as the k and ω equations of the SST. Three correlations are required to complete the model for γ-Re_θ: $Re_{\theta t}$, $Re_{\theta c}$ and F_{length}. Menter et al. [45] presented the relationship between $Re_{\theta t}$, the momentum thickness Reynolds number at which skin friction begins to increase, and $Re_{\theta c}$, the momentum thickness Reynolds number at which intermittency begins to increase for the first time. The closure of the model is dependent on expressions for $Re_{\theta c}$ and F_{length} that are functions of the transferred transition momentum thickness Reynolds number ($\tilde{R}e_{\theta t}$). Malan et al. [46] conducted both physical intuition and numerical experiments for plausible correlations of these forms. Where they reasoned that $\tilde{R}e_{\theta t} = Re_{\theta t}$ in the freestream was intended. The transport equations are some of the SST k-ω model as described by Menter [47] but with a slight modification and addition of two extra transport equations for the use of γ-Re_θ.

For the turbulent kinetic energy k,

$$\rho \frac{D(k)}{Dt} = \frac{\partial}{\partial x_j}\left[(\mu + \sigma_\kappa \mu_t)\frac{\partial \kappa}{\partial x_j}\right] + \left(\gamma_{eff}\mu_t S^2 - \rho\kappa\frac{\partial u_j}{\partial x_j}\right) - \min\left[\max(\gamma_{eff}, 0.1), 1\right]\rho\beta^*[1 + F(M_t)](\omega_k - \omega_0\kappa_0) \tag{12}$$

For the specific dissipation rate ω,

$$\rho \frac{D(\omega)}{Dt} = \frac{\partial}{\partial x_j}\left[(\mu + \sigma_\omega \mu_t)\frac{\partial \omega}{\partial x_j}\right] + \alpha\left(\mu_t S^2 - \rho\kappa\frac{\partial u_j}{\partial x_j}\right) - \rho\beta(\omega^2 - \omega_0{}^2) + 2\rho(1 - F_1)\sigma_{\omega^2}\frac{1}{\omega}\frac{\delta y}{\delta x_j}\frac{\delta \omega}{\delta x_j} \tag{13}$$

From the above equation, S is the strain rate tensor modulus, and γ_{eff} is the effective

intermittency. The ambient turbulence values are specified as quantities k (turbulent kinetic energy) and ω_k (specific rate of dissipation of turbulent kinetic energy), and they are used as source terms to suppress turbulence decay. Moreover, β^* and σ_κ represent turbulent Prandtl number and a coefficient related to the turbulent Prandtl number. $F(M_t)$ accounts for turbulent Mach number function and dilatation dissipation in incompressible flow. Where ρ is the density, u_j is the velocity vector, μ is the molecular viscosity, μ_t is the eddy viscosity, and F_1 is a function [46].

The γ- Re_θ transition model consists of two transport equations.

For the intermittency,

$$\rho \frac{D\gamma}{Dt} = \frac{\partial}{\partial x_j}\left[\left(\mu + \frac{\mu_t}{\sigma_\gamma}\right)\frac{\partial \gamma}{\partial x_j}\right] + F_{\text{length}}\, c_{a1}\rho S(\gamma F_{\text{onset}})^{0.5}(1 - c_{e1}\gamma) + c_{a2}\rho\Omega\gamma F_{\text{turb}}(1 - c_{e2}\gamma) \quad (14)$$

For transported transition momentum thickness Reynolds number,

$$\rho \frac{D\tilde{R}e_{\theta t}}{Dt} = \frac{\partial}{\partial x_j}\left[\sigma_{\theta t}(\mu + \mu_t)\frac{\partial \tilde{R}e_{\theta t}}{\partial x_j}\right] + c_{\theta t}\frac{(\rho U)^2}{500\mu}(Re_{\theta t} - \tilde{R}_{\theta t})(1 - F_{\theta t}) \quad (15)$$

where U is the magnitude of the local velocity and Ω is the vorticity tensor modulus. The length and position of the onset of the transition are controlled by the parameters F_{lenght} and F_{onset} respectively. The parameters for regulating the breakdown of the boundary layer and the boundary layer detector, respectively, are F_{turb} and $F_{\theta t}$. For γ and $Re_{\theta t}$, Neumann (zero-flux) wall boundary conditions are applied. At inlets, $\gamma = 1.0$ and $\tilde{R}_{\theta t}$ is obtained from the freestream correlation for $Re_{\theta t}$ [45]. The terms σ_ω, $\sigma_{\theta t}$, c_{a1}, c_{a2}, c_{e1}, c_{e2}, and $c_{\theta t}$ are coefficients that appear in the convective terms of the equation.
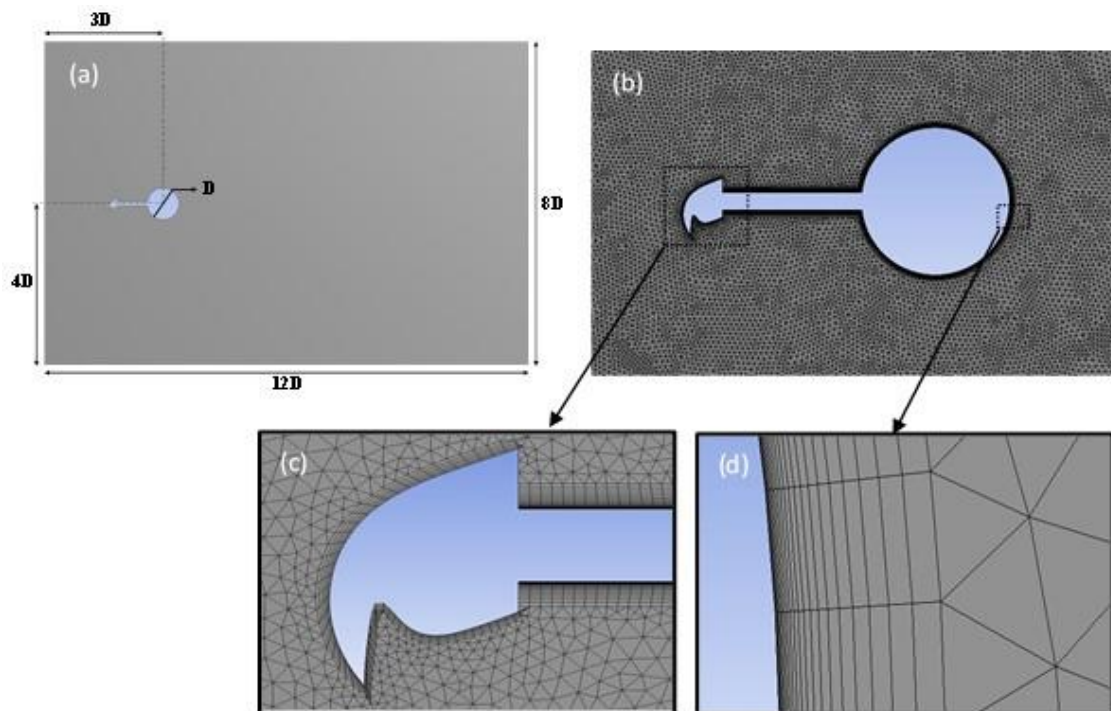
3.2. Geometry and meshing

Figure 4. (a) Extended surface with the cylinder in the fluid domain, (b) Meshing of the domain, (c) Zoom view of the extended surface mesh, (d) Zoom view of the mesh.

In the numerical study, a fluid domain was considered based on the bare cylinder diameter as shown in Figure 4.

The mesh for both the bare cylinder and the Peregrine Falcon was done in an unstructured mesh type with inflation, as shown in Figures 4(c) and 4(d). In the simulation study, $y^+ = 1$ was used for the subcritical Reynolds number. The y^+ represents a nondimensional distance of the first boundary layer from the no-slip wall.

3.3. Boundary conditions and solution control

Four different Reynolds numbers are used to calculate the inlet velocity for uniform flow for the study on the bare cylinder. Inlet velocities for the corresponding subcritical Reynolds number were computed. As the chosen Reynolds number transitions from laminar to turbulent, the flow solver Transition SST k-ω model was utilized in the computation. Among the pressure-velocity coupling algorithms, the 'Coupled Algorithm' was chosen. The simulations were done for about 10 seconds, and the turbulent intensity was according to the wind tunnel situation.

3.4. Grid independence test

A grid independence test was done to identify the optimum grid size. An optimum grid size is necessary for proper boundary layer separation. At first, it was a simulation at $Re = 1 \times 10^4$, and then gradually, the node number or element size was increased to refine the mesh. As shown in Figure 5, by increasing the node's number, the drag coefficient reduces to a point where it remains mostly constant.
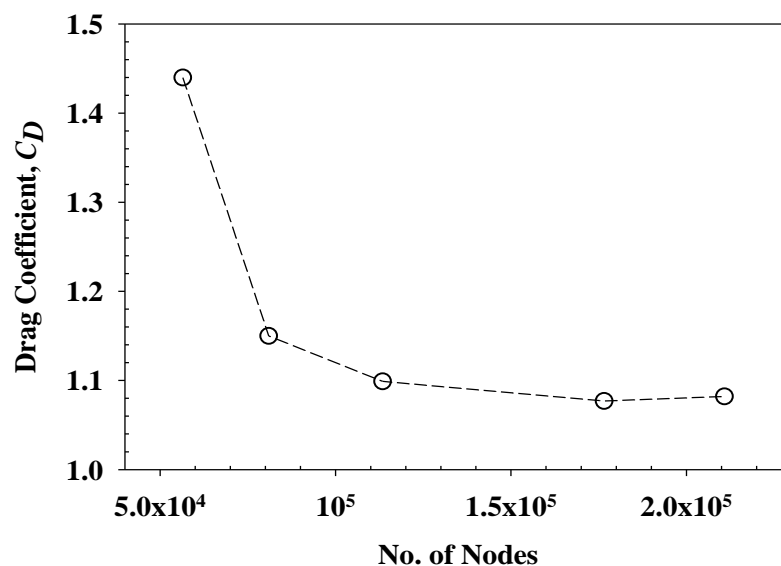

Figure 5. Drag coefficient, C_D variation with the increase of No. of nodes.

The node number 176539 is considered for the simulation study, where it has $C_D = 1.07$ at $Re = 1 \times 10^4$, which is almost the same as the node number of the 210821, and most importantly, it takes less computational time than the higher nodes. Using the grid independence test, the correct mesh properties were identified, and numerical simulations for Reynolds numbers between 5.67×10^4 and 1.79×10^5 were performed using the same mesh properties.

3.5. Verification and validation

For verification and validation, the bare circular cylinder experimentation was compared with experimentation done on a smooth cylinder by Munson et al. [48]. Furthermore, the simulated result of the bare cylinder drag coefficient, C_D , was compared with other simulated available literature like Stringer et al. [40], Rosetti et al. [49], and Yuce and Kareem [50]. On the other hand, the experimental result was also compared by Hoener [51], Achenbach [52], Hojo [53], and Zdravkovich [7]. All the comparison with the literature is illustrated in Figure 6. It is observed that there are discrepancies between simulations and experimentations, especially for Reynolds numbers 5.67×10^4 to 1.79×10^5 as this range is the transition from laminar to turbulent. This region causes a lot of discrepancies due to boundary layer separation happening uncertainly leading to a laminar separation bubble being generated [54]. Hence, these bubbles cause a substantial amount of difference from the simulation result. In addition, the simulations were conducted in 2D simulation as these results are not able to capture the whole aspect of the real three-dimensional object. However, better results may be obtained with more computational power and with a more refined mesh.
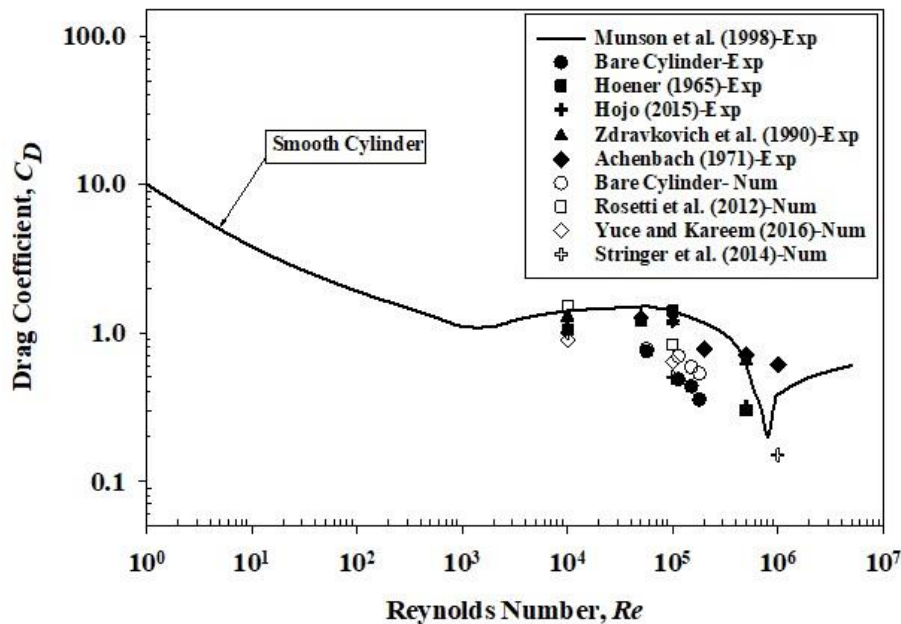

Figure 6. Comparison of bare cylinder drag coefficient with numerical and experimental results for different Reynolds numbers.

4. Results and discussions

4.1. Experimental results

4.1.1. Experiments on the whole Peregrine Falcon

Inspired by nature, the whole Peregrine Falcon model (WF) is used to investigate the drag coefficient for a wide range of Reynolds numbers. In addition, six different angles of attacks (−20º, -

10º, 0°, 10°, 20°, and 30°) are tested and compared with the bare cylinder (BC), as shown in Figure 7(a). The results show that the whole Falcon's drag coefficient is much lower than the bare cylinder. A significant issue is that at the low Reynolds number region, the whole Falcon model exhibits much lower C_D values. The differences between the bare cylinder and the whole Falcon model are much reduced with the increase of the *Re* values. Low Reynolds numbers with 10° and 20° angle of attack have shown similar results; however, 0° angle of attack has more consistent results in drag coefficient for a wide range of Reynolds numbers. However, it should be noted that the negative angle of attacks shows a detrimental effect on the drag coefficient for the whole Falcon model. The lowest drag coefficient is found to be around 0.18 for the angle of attack 20° at $Re = 5.67 \times 10^4$. Ponitz et al. [37] reported the diving Falcon could have a drag coefficient as low as 0.094 for the $Re = 5.9 \times 10^5$ with an angle of attack of 5°. In the present study, it was not possible to attain such *Re* for the Falcon model due to some limitations of the wind tunnel. However, the experimental results depict that C_D could be much lower and much reduced with the increase of the Reynolds number, and there is a huge variation of C_D for the low *Re* values as compared with the bare cylinder, which can assist in many applications.

4.1.2. Experiments on the moderate Falcon model

Having a much lower drag coefficient for the whole Falcon model (WF), especially on low Reynolds number, the Falcon model is modified as a moderate Falcon model (MF), as shown in Figure 1(d), where the extended surface is completely connected with the main cylinder. In this study, seven different angles of attack (−20º, −10°, 0°, 10°, 20°, 30°, and 40°) for different Reynolds numbers are tested. Figure 7(b) shows that the 0° angle of attack shows a much lower C_D for the entire range of *Re*. It should be noted that the higher angle of attack has a detrimental effect on C_D. Indeed, from Figure 7(b), at a 40° angle of attack, the moderate Falcon has the highest drag coefficient, and reducing the angle of attack helps to reduce the drag coefficient. A 0° angle of attack had the lowest drag coefficient $C_D = 0.21$ at 5.67×10^4 Reynolds number. The most significant finding is that the drag coefficient is significantly decreased for the low Reynolds number and almost uniform for the tested Reynolds number range. This finding is not found for bare cylinders. Indeed, the moderate Falcon model reduced the drag coefficient by making a streamwise flow pattern over the structure.
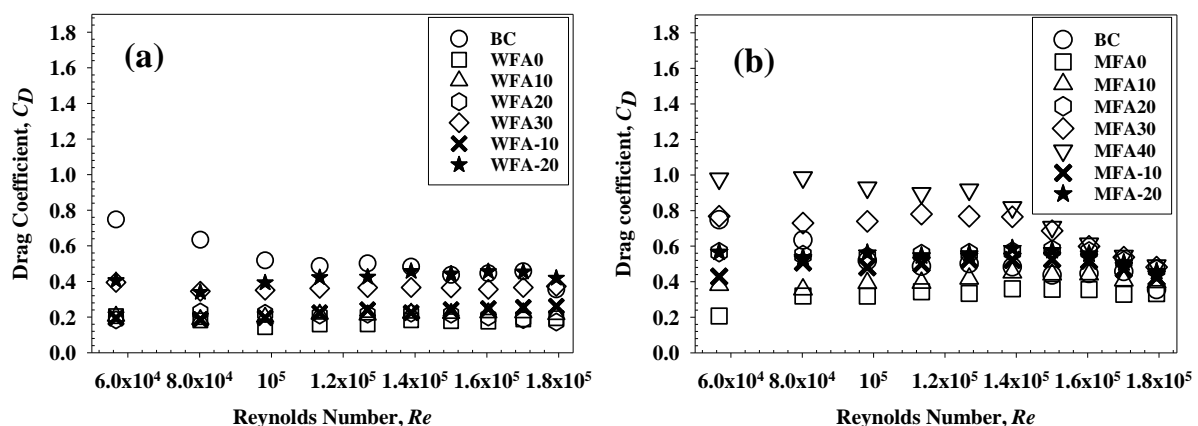

Figure 7. Drag coefficient measured from the experimental data for different Reynolds numbers with different AOA (a) whole Falcon, and (b) moderate Falcon.

4.1.3. Experiments on extended surface model

Further experimental studies are carried out with the extended surface where the extended surface is considered the beak of the Falcon, as explained earlier in Figure 1(c). Experimentations are done for 15 cases where the diameter of the cylinder is fixed, and the three different stem lengths 60, 70, and 80 mm with the $L/D = 0.97$, 1.09, and 1.20, respectively, where L is measured as the total length of stem length and the beak length, with five different angles of attacks (0°, 10°, 20°, 30°, and 40°) for each stem length. It should be noted here that during the experiments, the L/D was tried to keep close as per the real case, as the leading edge of the beak of a Falcon is approximately 0.93 times ahead of the body. All the cases are carried out for on the Reynolds numbers ranging from 5.67×10^4 to 1.79×10^5. The cases are defined with unique notations, like in the notation S80A0, 'S' stands for a stem length of 80 mm, and 'A' stands for an angle of attack of 0° with a fixed diameter of 85 mm for all cases.
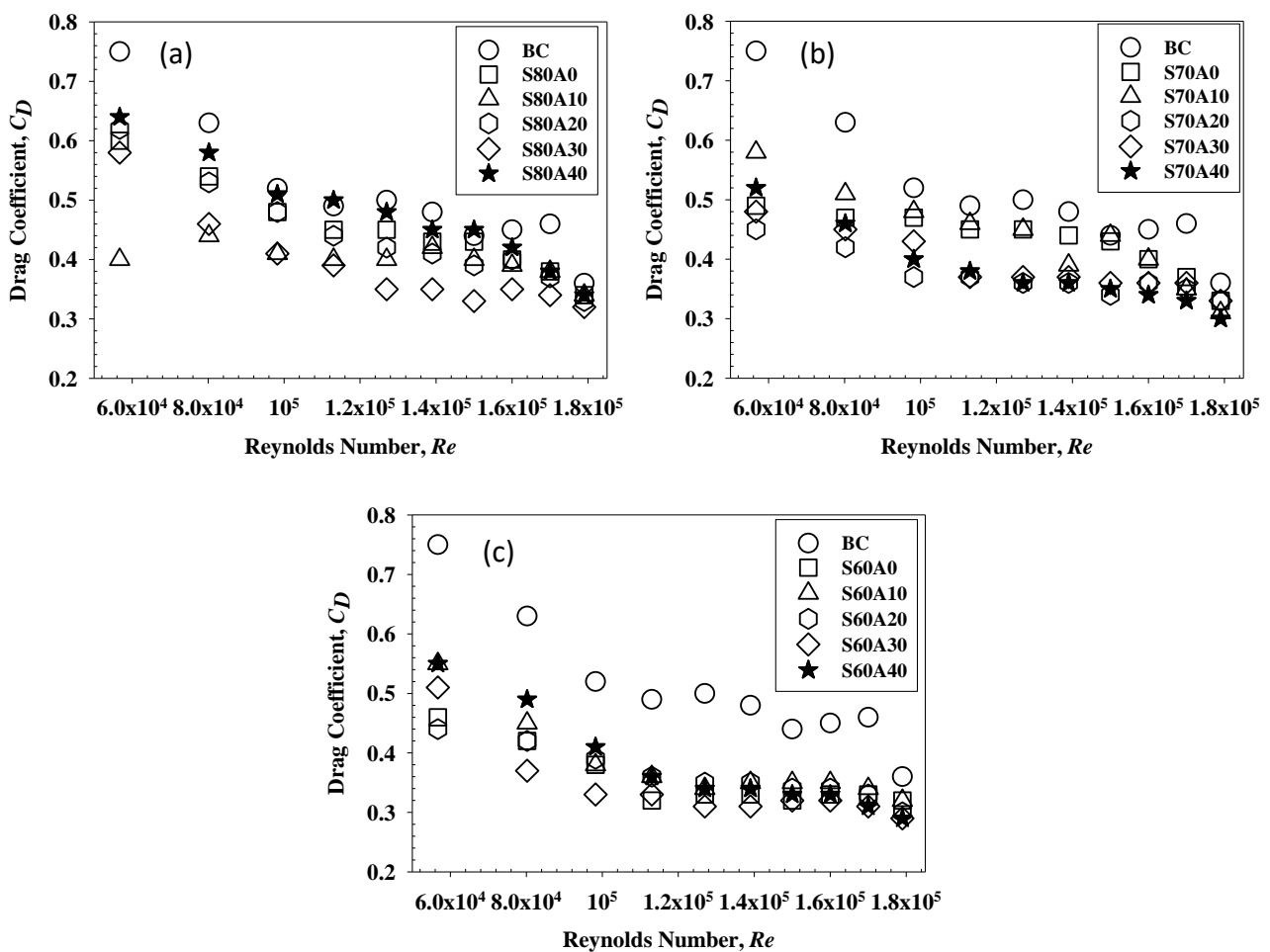

Figure 8. Drag coefficient measured from the experimental data for the extended surface model at different AOA for stem length (a) 80 mm ($L/D = 1.20$), (b) 70 mm ($L/D = 1.09$), and (c) 60 mm ($L/D = 0.97$).

Figure 8 shows the variation of the drag coefficient for different Reynolds numbers where three different stem lengths are chosen with a wide range of angles of attack. Due to laminar separation

bubbles, the drag coefficient is high at a low Reynolds number for each stem length. This bubble causes vortices behind the extended surface and ultimately increases drag. It is evident from Figure 8 that the drag coefficient is significantly dependent on the stem length and angle of attack for different Re values. Indeed, for low Re, a longer stem length with a lower angle of attack exhibits a low drag coefficient, and for high Re, a shorter stem length with a higher angle of attack has a lower C_D. Eventually, the stem length, angle of attack, and cylinder diameter are all issues that make an interdependency for the drag coefficient [29].

Now, comparing all the cases, the whole Falcon model exhibited the lowest drag coefficient. However, the moderate Falcon model and the extended surface with a certain stem length showed a much lower drag coefficient as compared with the bare cylinder. The comparisons of the drag coefficient of all the cases at 0° angle of attack, which is the direction of fluid flow, are shown in Figure 9.
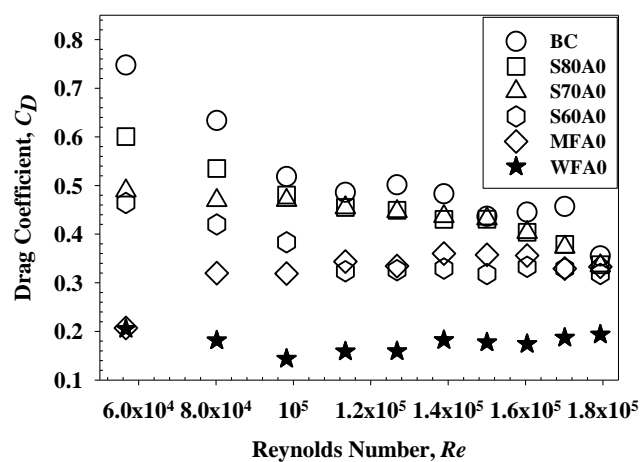

Figure 9. Comparison of different models at AOA = 0°.

From Figure 9, the drag coefficient reduces for every case as compared with the bare cylinder (BC). Among the three stem lengths at an angle of attack of 0°, 60 mm reduces the most up to 0.3 at a high Reynolds number. However, both the Moderate Falcon 'MFA0' and the Whole-body Falcon model 'WFA0' have the lowest drag coefficient at a 0° angle of attack, and the lowest drag coefficients found for the two in the individual cases were $C_D = 0.21$ at $Re = 5.67 \times 10^4$ and 0.14 at $Re = 9.82 \times 10^4$, respectively. The reason for having higher C_D values for the extended body case may be the formation of the vortices in between the extended surface and the main body. In that case, placing an extended surface at the upstream position of the main cylinder can be taken positively to reduce the drag. On the other hand, the whole-body Falcon models having the lowest drag can be attributed to having a streamwise flow pattern and, indeed, disrupting vortices during the flow at the downstream position. In Figure 9, the Falcon model for different stems' drag coefficients is shown. Here, S80A0 denotes a Falcon model with a stem length of 80 mm and an angle of attack of 0°. WFA0 and MFA0 denote the whole Falcon and moderate Falcon with the angle of attack of 0°, respectively.

4.2. Percentile of drag reduction

To investigate the drag reduction by attaching an extension on the bare cylinder, the percentage of drag coefficient reduction of the configuration (i.e., with the extended surface) is calculated based

on the drag coefficient of the bare cylinder as $\left(\frac{\Delta C_{Dc}}{C_{Db}}\right)$, where C_{Dc} is the drag coefficient of the configuration because of extended surfaces and C_{Db} is the bare cylinder drag coefficient. As shown in Eq. 16.

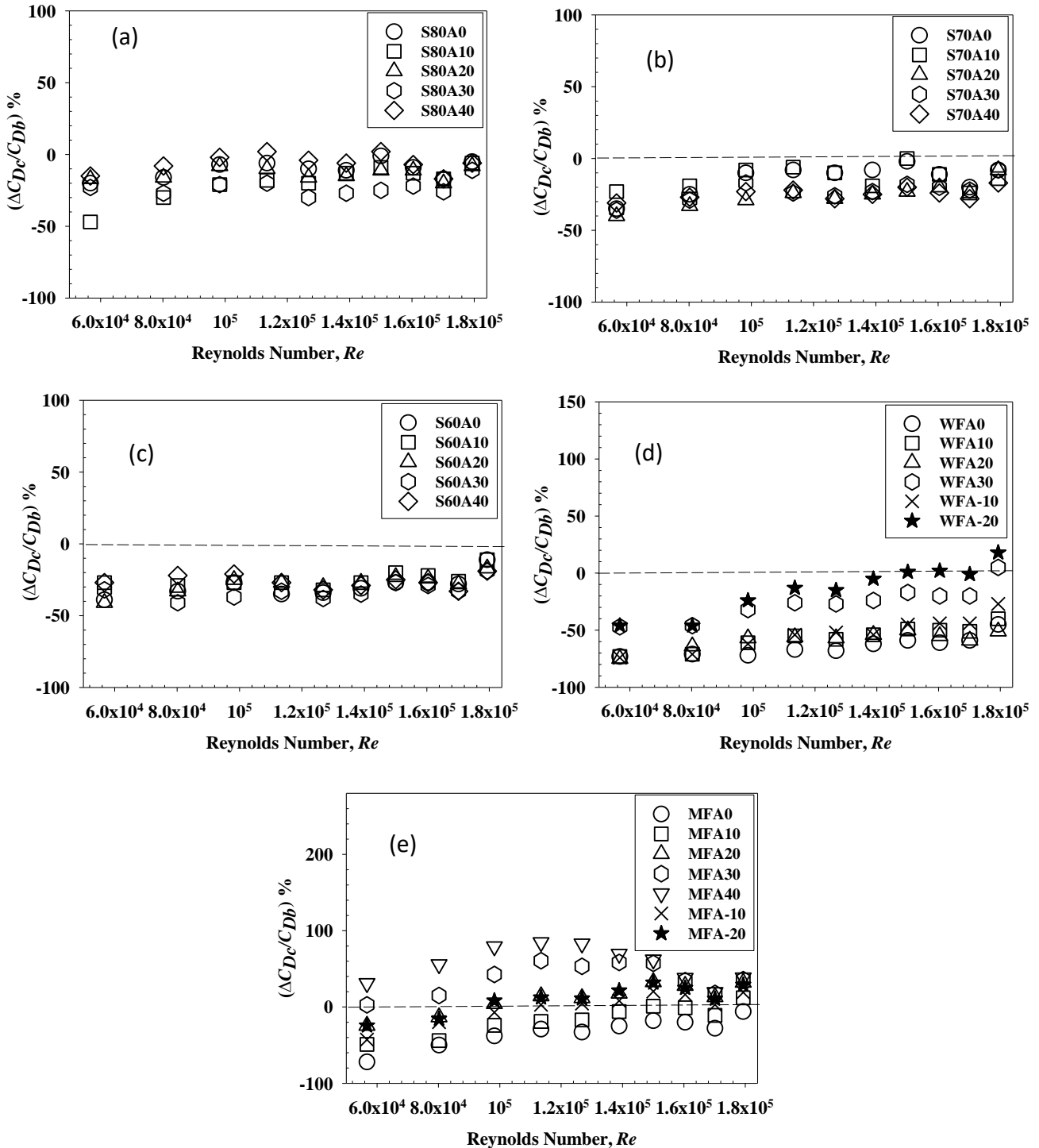$$\left(\frac{\Delta C_{Dc}}{C_{Db}}\right) = \frac{C_{Dc}-C_{Db}}{C_{Db}} \times 100\% \tag{16}$$

Figure 10. Experimental percentile of drag reduction of the extended surface model with stem length (a) 80 mm (L/D = 1.20), (b) 70 mm (L/D = 1.09), (c) 60 mm (L/D = 0.97), (d) whole Falcon, and (e) moderate Falcon.

The percentile drag reduction for different configurations is shown in Figure 10. From the stem length variations depicted in Figure 10(a), (b), and (c), the most significant reduction in drag, approximately 47%, was seen for a stem of 80 mm ($L/D = 1.20$) at an angle of attack of 10°. Nevertheless, despite stem 80 mm having the lowest percentage, the majority of drag reduction was attained with stem 60 mm, where the majority of drag reduction was more than 20% at all angles of attack. One of the major findings is that the 60 mm stem length ($L/D = 0.97$) has the same consistent percentile drag reduction as the whole Falcon model with the positive angles of attack (see Figure 10(d)), whereas the moderate Falcon model is inconsistent in percentile drag reduction as it is also observed for the 70 and 80 mm stem lengths, or $L/D = 1.09$ and 1.20, respectively (see Figure 10(e)).

The percentile of drag reduction of the extended surface in minimizing the drag is due to the interaction of separation flow between the extended surface and the cylinder. As the extended surface is based on the shape of a Peregrine Falcon's beak, boundary layer separation occurs at the extended surface and reattachment on the cylinder, particularly downstream of the cylinder. Indeed, there is no definite stagnation point of the cylinder, where the pressure coefficient is greatest, and drag is the most substantial. A significant factor here is the beak's streamlined design, which acts as the extended surface and eventually comes into contact with the free stream flow at that position, enhancing to reducing the drag. Therefore, placing the extended surface at the upstream position of the cylinder, the beak creates a smooth and aerodynamic surface that reduces turbulence and separation of the air passing over the cylinder. This can reduce the magnitude and intensity of the vortices and wake formed behind the cylinder

Varying the distance between the extended surface and the circular cylinder can have a substantial effect on the cylinder's drag. Indeed, when the extended surface is positioned near the cylinder, the airflow between the two surfaces can be restricted, increasing drag. This is because the air flowing between the surfaces can generate turbulence, vortices, and low-pressure regions that increase the cylinder's resistance to motion. When the extended surface is further away from the cylinder, however, the movement of air between the two surfaces can become smoother and more laminar. Reducing the turbulence and vortices created in the airflow around the cylinder can help reduce drag. There is, however, an optimal distance between the extended surface and the cylinder that maximizes the drag reduction. This distance will depend on variables such as the size and shape of the cylinder and the extended surface, the speed and direction of the airflow, and the surface materials. As an extended surface, the beak of a peregrine falcon is effective at reducing drag due to its streamlined and slim profile. One of the fundamental principles in the study of aerodynamics is that the amount of drag experienced by an object is directly proportional to the square of its velocity and is also affected by its shape, especially the frontal part, and hence the flow separation. The falcon's beak, featuring a diminished leading edge, efficiently reduces the cross-sectional area that encounters the incoming air, resulting in effective reattachment to the cylinder and thus minimizing drag. The design bears resemblance to the streamlined fuselage of aircraft, highlighting the significance of reducing frontal area to enhance aerodynamic performance. Additionally, the beak of the falcon is extremely tapered and pointed, which serves to minimize the size of the leading edge and reduce the pressure wave produced when air travels around an object. As this pressure wave can cause drag, minimizing its magnitude can also assist in reducing drag. Moreover, the beak's pointed design serves to reduce the creation of shock waves and pressure disturbances. As the beak glides through the air, the reduction in sudden fluctuations in airflow aids in diminishing the strength of the pressure waves produced. This is

consistent with the idea of optimizing to decrease both form drag (drag caused by an object's shape) and wave drag (drag related to pressure waves).

The formation of a boundary layer of air over the surface can be considered another factor for the reduction of the drag coefficient. Due to the nonslip nature of the fluid, a thin layer of air forms along the surface as air flows over the beak and cylinder. This boundary layer can aid in reducing the thickness of the turbulent boundary layer that forms further from the cylinder's surface, thereby aiding in the reduction of drag. The size and design of the beak would also contribute to the reduction of drag. Curvature and angle of the upper mandible of the beak, as well as the tapered and pointed shape of the beak, may aid in guiding the passage of airflow over the surface of the cylinder in a manner that reduces turbulence and separation, weakening the wake region at the downstream of the cylinder. Also, at lower Reynolds numbers, the flow tends to be more laminar, while at higher Reynolds numbers, it becomes increasingly turbulent. The size and design of the beak, particularly the curvature and angle of the upper mandible, contribute to the manipulation of the Reynolds number and, consequently, the flow regime. A streamlined and pointed beak shape can help maintain laminar flow and delay the onset of turbulence. Furthermore, the separation of the boundary layer on the extended surface causes the formation of vortices between the extended surface's gap (stem length) and the cylinder [55]. As the gap or stem length increases, so do the size of the vortex pair and the amount of vortex formation, leading to vortex separation and more significant drag. Due to the shorter length of the 60 mm stem in comparison to the 80 mm and 70 mm stems, most of the drag was minimized. In the case of the whole Falcon and moderate Falcon, the whole Falcon at $Re = 5.67 \times 10^4$ for 0°, 10°, 20°, 30°, −10°, and −20° the percentage of drag reduction was about 73%, 73%, 75%, 47%, 74%, and 46%. Thus, at a 20° angle of attack, the whole Falcon model achieved the highest drag reduction, but for the remaining range of Re from 8.02×10^4 to 1.79×10^5 most drag was reduced at 0° angle of attack in contrast to all the rest of the angles of attack. This is due to the whole Falcon having an aerodynamic shape enabling it to have the fluid flow effectively and generate proper streamlines. On the other hand, the moderate Falcon also has a significant reduction reaching about 72% at 0° of the angle of attack, and most of the reduction happens at that respective angle of attack. Additionally, in the moderate Falcon model, as the angle of attack and Reynolds Number increase, the percentile of drag reduction turns into a positive value which means drag increases rather than reduces. At 0° of the angle of attack, the moderate Falcon retains somewhat the aerodynamic shape of the whole Falcon, so it has the same result of lowering drag as the whole Falcon. However, as an angle of attack is introduced, the fluid cannot flow effectively, especially upstream and downstream of the cylinder resulting in higher drag. For such cases, real-life Peregrine Falcon tail comes into consideration, as found in the literature [37]. The tail end works in such a way that the fluid can flow smoothly and ensures the wake generation is disrupted, resulting in low drag.

As a result, for a wide range of Reynolds numbers, both the moderate Falcon model and the extended surface can be considered aerodynamic in different applications. Such a shape can be effectively implanted in the front of a car, ship, or other floating body.

4.3. Numerical results

Based on the percentile drag reduction few computational fluid dynamics studies are being conducted further to study the flow characteristics of the extended surface to understand the aerodynamic issues of drag reduction. Three cases are considered for the numerical simulation to

understand the flow pattern better and compare the experimental results with the simulation results. Table 1 shows the drag coefficient comparison of the three extended surface models for the three different Reynolds numbers 5.67×10^4, 1.27×10^5, and 1.70×10^5, respectively. Two angles of attack are selected based on the lowest drag at the lowest Reynolds number, and simulations were conducted in that range. It is clear from Table 1 that the numerical and experimental C_D values for all the cases are very close to the higher Reynolds number. There are some discrepancies in C_D values for the low Reynolds number, which may be due to the transition of the laminar to the turbulence of the flow.

Table 1. Experimental/numerical C_D values due to extended surface simulation of the Peregrine Falcon model at three different *Re*.

Re	S = 80 mm (*L/D* = 1.20)				S = 70 mm (*L/D* = 1.09)				S = 60 mm (*L/D* = 0.97)			
	A-0		A-10		A-0		A-20		A-0		A-20	
	Exp	CFD	Exp	CFD	Exp	CFD	Exp	CFD	Exp	CFD	Exp	CFD
5.67×10^4	0.60	0.71	0.40	0.43	0.49	0.38	0.45	0.50	0.46	0.41	0.44	0.51
1.27×10^5	0.45	0.38	0.40	0.39	0.45	0.37	0.36	0.46	0.33	0.35	0.35	0.44
1.70×10^5	0.38	0.37	0.38	0.38	0.37	0.34	0.35	0.45	0.33	0.34	0.33	0.44

As the comparison is given in the table above, the chosen situations are further detailed to emphasize the benefits of employing the extended surface. Thus, the vortex behind a bare cylinder, a cylinder with a 60 mm stem, and a cylinder with an 80 mm stem are shown in Figure 11 at a high Reynolds number, $Re = 1.70\times10^5$.

Figure 11 shows the generated vortex behind the cylinder with a stem length of 60 mm and 80 mm for $Re = 1.70\times10^5$ and compared with the bare cylinder for AOA = 0°. The drag coefficients are much reduced in these two cases as compared with the bare cylinder. The sizes of the vortices are reduced and stretched along the flow direction significantly behind the cylinder as compared with the bare cylinder, as shown in Figure 11(a) – (c), which have a lower drag coefficient. However, comparing the 60 mm and 80 mm cases, the 60 mm stem length has a slightly lower drag coefficient. To find the reason for having a lower drag coefficient of 60 mm, the flow patterns between the falcon beak and cylinder are shown in Figure 11(d) and (e). It is observed that the vortices, which are also termed quasi-steady vortices [19] for both the upper and lower portions, are much stretched along the flow direction for the 80 mm stem length. The reattachment to the cylinder occurs at a greater angle due to the longer stem length. Furthermore, the quasi-steady vortex region contributes significantly to the shear layer, lowering pressure downstream of the cylinder [19]. Therefore, the stretching of the vortices is due to the longer length of the stem, which affects the reattachment on the cylinder, and eventually, the vortex sizes increase. However, the length of the stem or the gap between the extended surface and the cylinder is one of the major influencing factors for wake formation and hence the drag reduction [29,55].
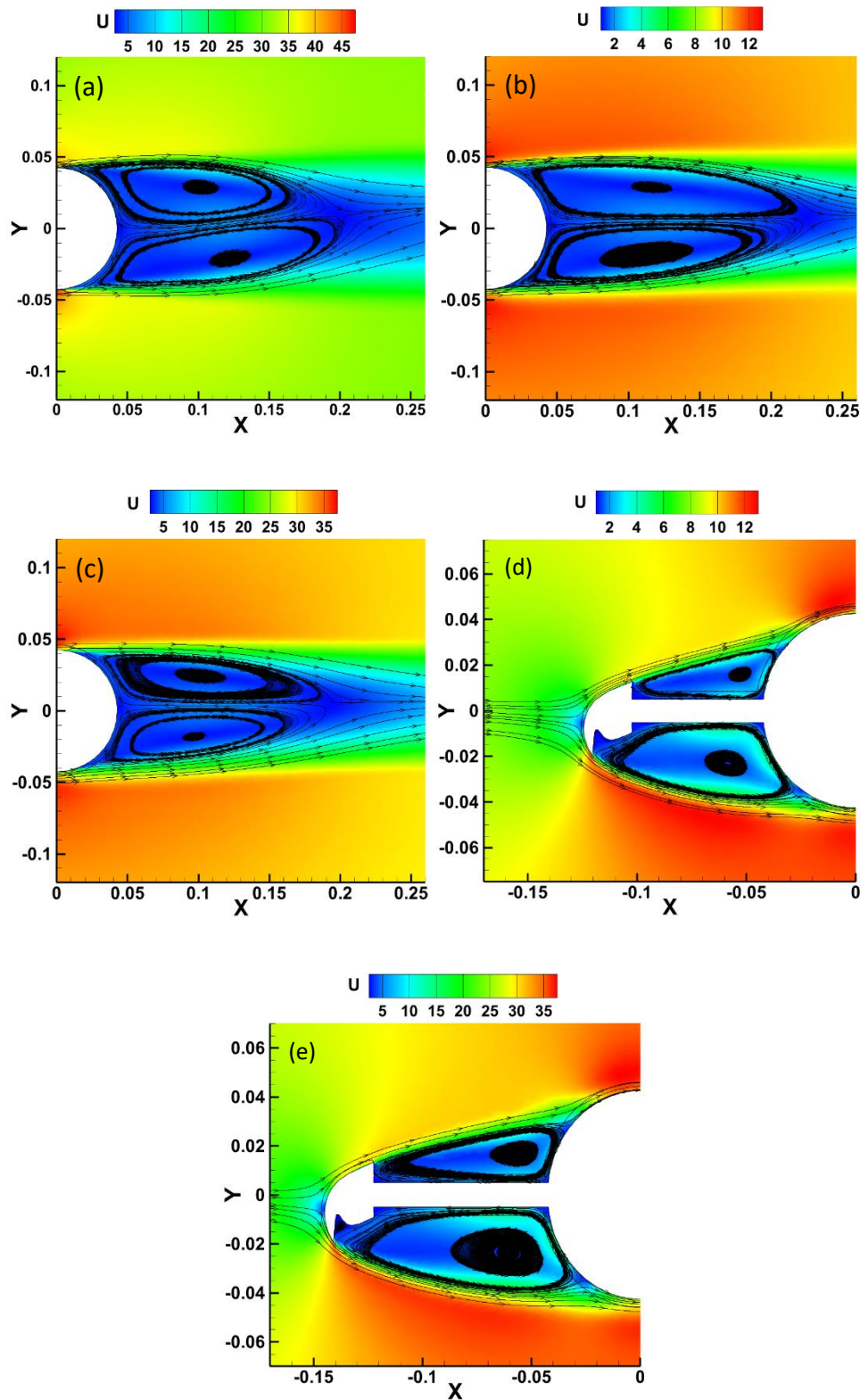
Figure 11. Velocity contour at $Re = 1.70 \times 10^5$ with streamlines for behind (a) bare cylinder, (b) cylinder with 60 mm stem, (c) cylinder with 80 mm stem, and in front of cylinder with (d) 60 mm stem, and (e) 80 mm stem.

4.3.1. Flow field velocity

To investigate the influence of the extended surface and stem length, velocity distributions are observed at different downstream positions of the cylinder. Indeed, four positions are selected at X/D = 0.5, 1, 1.5, 2 as shown in Figure 12.
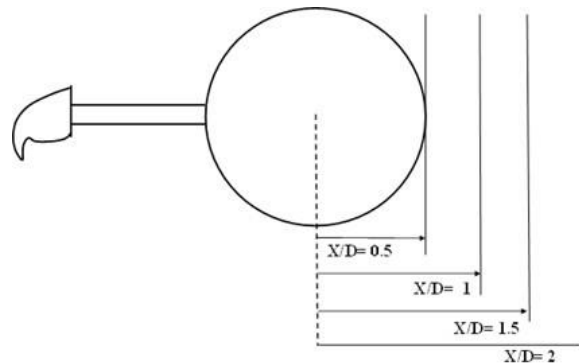
Figure 12. Diagram of lines positioned for velocity distribution.

Figure 13 shows the velocity distribution (U/U_∞) at different downstream positions for several cases, and the y-axis depicts the vertical scaling where both the positive (+ve) and negative (-ve) y directions represent the upward and downward positions of the respective figures. For instance, Figure 13(a) shows the velocity distribution at $Re = 5.67 \times 10^4$ for the bare cylinder and easily depicts that the flow patterns are symmetric concerning the y-axis. The shape of the U/U_∞ resembles each other in the y-direction for various X/D positions; however, X/D = 0.5 differs from the other positions because it is the closest and contacts the cylinder. Immediately, after the cylinder, the flow pattern is in a 'U' shape and changes to a 'V' shaper as going for the further downstream positions. Aguedal et al. [56] and Yan et al. [22] reported similar observations. On the other hand, for the same Reynolds number, while the extended surfaces are placed in front of the cylinder at 60 mm ($L/D = 0.97$) and 80 mm ($L/D = 1.20$), respectively, the velocity profiles become asymmetric (Figure 13(b) and (c)), and the velocities are much reduced in the y direction, especially at the lower side of the cylinder. The tendencies of reducing the velocity in the flow direction and also lateral directions are reported in several kinds of literature like Ji et al. [57], and Qi et al. [58] and this causes a higher pressure behind the cylinder, resulting in a lower drag coefficient as compared with the bare cylinder. Comparing the obtained drag coefficients, the 60 mm stem length ($L/D = 0.971$) had a lower drag coefficient as compared with the 80 mm ($L/D = 1.20$). This may be the formation of a strong vortex between the beak and cylinder, as explained in Figure 11. Considering the changes in the angle of attack from 0º to 20º (Figure 13(b) and (d)) for the same Reynolds number and stem length, velocity is consistently reduced in the y direction and reduced the drag. However, the results indicate that the vortex shifted to a further upward position (i.e. +ve y direction) for a higher angle of attack, and velocity resembles having a constant in the +ve y direction for different downstream positions and a lower velocity in the -ve y direction and ultimately resulting in a slight improvement in drag coefficient. Considering the same case as shown in Figure 13(d), the Reynolds number is increased to 1.70×10^5 and the velocity distributions are shown in Figure 13(e). In this particular case, the drag coefficient slightly increased due to the variation of the velocity distribution both in downstream and vertical directions.
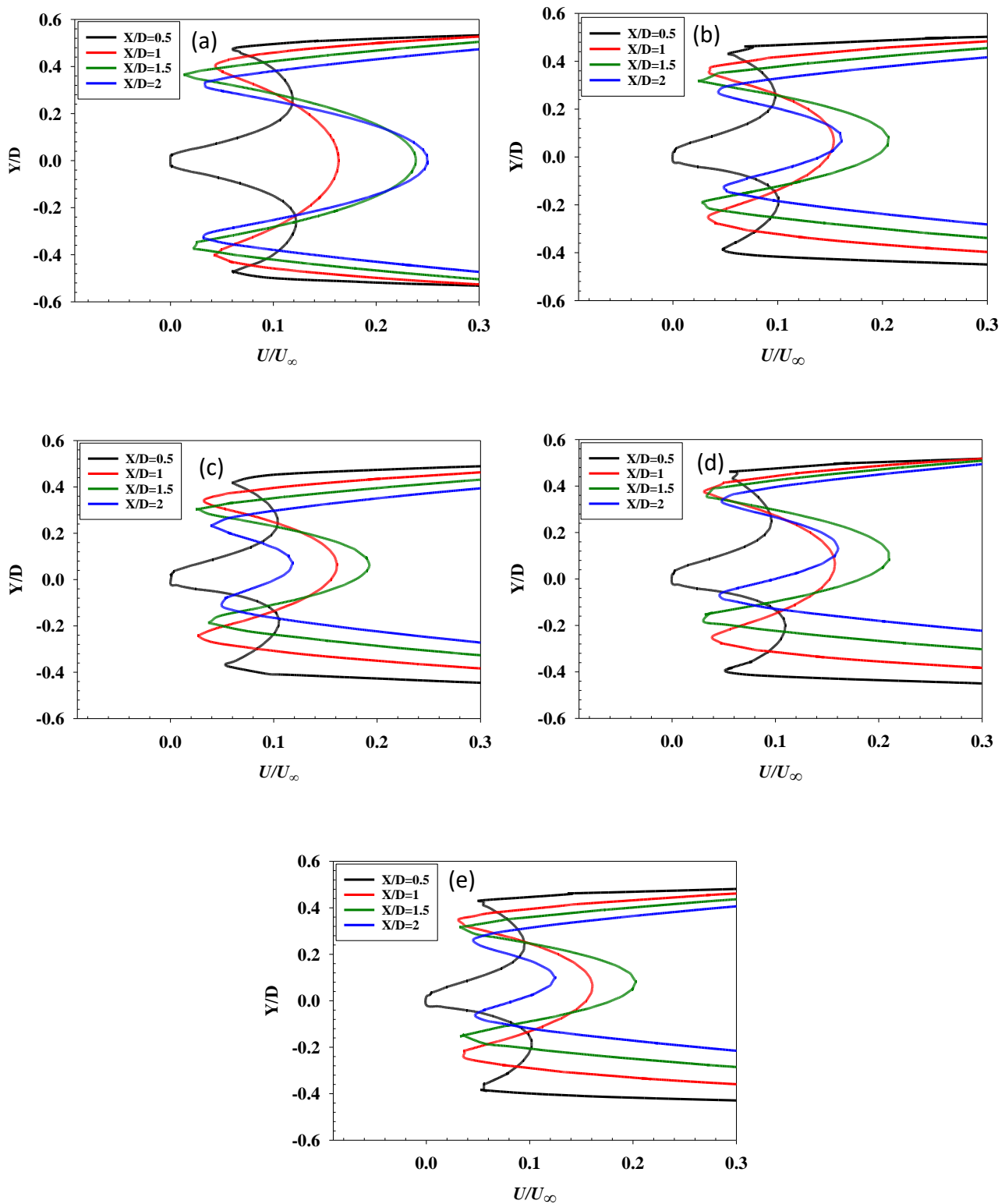
Figure 13. Velocity distribution behind circular cylinder under different X/D conditions for Re = 5.67×104 (a) bare cylinder, (b) 60 mm stem length, and (c) 80 mm stem length, 60 mm stem length with AOA = 20o at (d) Re = 5.67×104 (e) Re = 1.70×105.
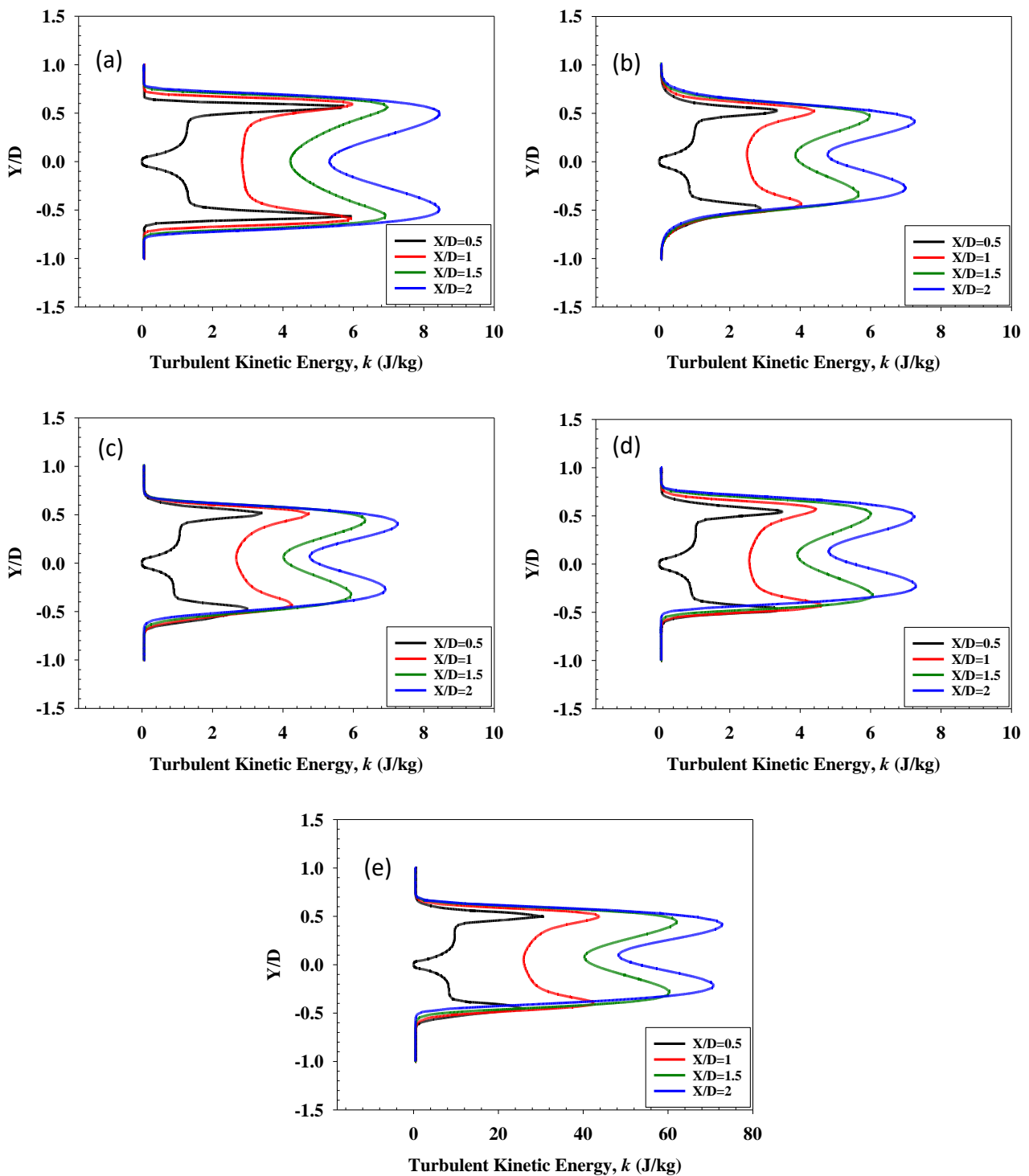
4.3.2. Turbulence kinetic energy

Figure 14. Turbulent Kinetic Energy (k) behind circular cylinder under different X/D conditions for Re = 5.67×104 (a) bare cylinder, (b) 60 mm stem length, and (c) 80 mm stem length, 60 mm stem length (L/D = 0.97) with AOA = 20o at (d) Re = 5.67×104 (e) Re = 1.70×105.

The kinetic energy is associated with turbulent eddies and is known as turbulent kinetic energy (TKE i.e. *k*), and a value for turbulent kinetic energy with a higher magnitude indicates a more

turbulent flow. The wake vortices are produced by the flow's turbulent kinetic energy; as this energy decreases, the generation of the vortices is reduced as well, leading to a higher energy flow recovery and a reduction in drag. The turbulent kinetic energy distributions behind the circular cylinder with different cases are illustrated in Figure 14. The pattern of distribution of the k for the bare cylinder is symmetric concerning the y-axis; however (see Figure 14(a)), the k is increased in the downstream positions. The noticeable thing is that the k is much higher in the vortex periphery. However, the turbulent kinetic energies are decreased for the cylinder with the extended surface for both 60 mm and 80 mm stem lengths as shown in Figure 14(b) and (c). It should be noted here that due to the asymmetric nature of the beak of the extended surface, the shear layer leads to an increase in the k in the +ve y direction and depicts highly turbulent flow as compared with the –ve y direction. The lower k values and smaller turbulent flow for the cylinder with the extended surface indicate that less flow energy is used for forming the vortices behind the cylinder, especially in the wake region. As a result, this leads to a lower drag force. Findings are consistent with the velocity distributions, as the angle of attack has a large influence on having an asymmetric flow pattern, as shown in Figure 14(d). The magnitude of the k is much increased for the higher Reynolds number, as depicted in Figure 14(e).
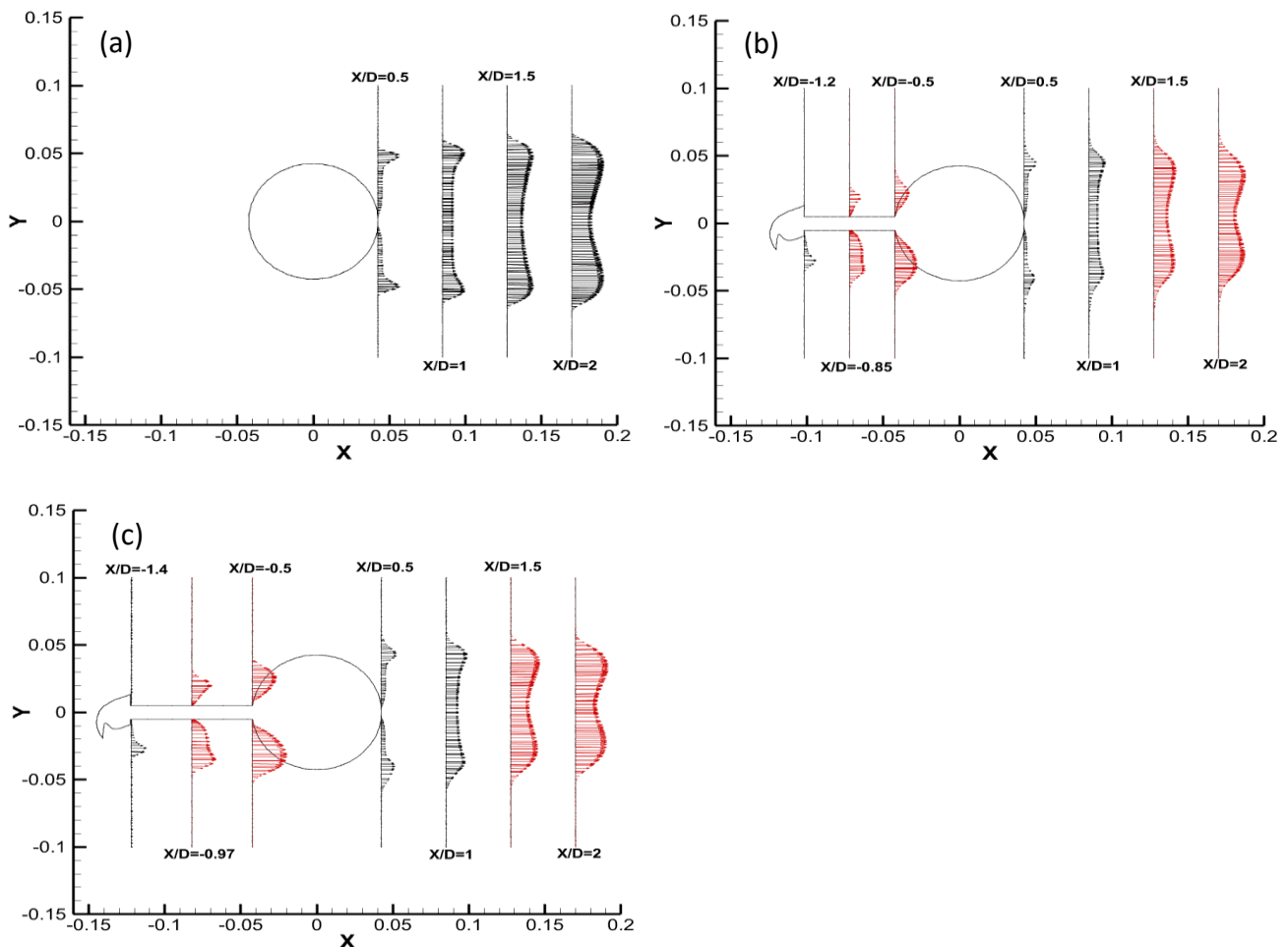

Figure 15. Turbulent Kinetic Energy (k) spatial distribution behind circular cylinder at different X/D positions for $Re = 5.67 \times 10^4$ (a) bare cylinder, (b) 60 mm stem length ($L/D = 0.97$), and (c) 80 mm stem length ($L/D = 1.20$).

The turbulent kinetic energy distributions around the cylinder within the flow domain are shown in Figure 15. Due to the asymmetric nature of the beak of the extended surface, the k distributions are shifted in the +ve y direction behind the cylinder for both the 60 and 80 mm stem lengths. However, a strong k is observed for the 80 mm stem length in between the beak and the cylinder as compared with the 60 mm stem length. Figures 15(b) and (c) demonstrate that the k value is significantly larger for a stem length of 80 mm, as indicated by the red rows. Therefore, reattachment occurs at a higher angle on the cylinder, as explained in Figure 11. It is observed from the figure that the k is much reduced behind the cylinder as compared with the bare cylinder, which leads to a lower drag coefficient with the extended surface.

5. Conclusions

Our primary objective of this extensive investigation was to decrease the drag coefficient by taking inspiration from the Peregrine Falcon, known for its exceptional ability to minimize drag during dives. Three unique geometric forms were analyzed: The whole Falcon model, the moderate Falcon model, and a cylinder with an extended surface resembling a Falcon's beak. The testing included subsonic wind tunnel experiments and 2D numerical simulations conducted over a wide range of Reynolds numbers. The following observations can be highlighted based on experimental and numerical studies:

- The whole Falcon model displayed the most minimal drag coefficient, achieving a value of 0.18 at a Reynolds number of 5.67×10^4 and an angle of attack of 20°. A significant decrease in drag of up to 75% was seen as compared to the bare cylinder, especially at positive angles of attack.
- The moderate Falcon model exhibited a significant reduction in drag of 72% when tested at a 0° angle of attack, with a Reynolds number of 5.67×10^4. The Falcon's beak-like extended surface showed varied drag coefficients but consistently outperformed the bare cylinder, particularly at low Reynolds numbers.
- Stem length had a substantial impact on drag; at $Re = 5.67 \times 10^4$ (angle of attack 10°), the 80 mm stem achieved an impressive 47% drag reduction.
- The whole Falcon model exhibited constant drag reduction across a broad spectrum of Reynolds numbers and angles of attack, in contrast to the moderate Falcon model.
- Comparing the whole Falcon model and the moderate Falcon model, the percentile drag reduction of the whole Falcon model is consistent for a wide range of Reynolds numbers and angles of attack. In contrast, percentile drag reduction is greatly influenced by the angles of attack and the Reynolds number for the moderate Falcon model.
- When comparing stem lengths, it is seen that the 60 mm stem length ($L/D = 0.97$) exhibits consistent drag reduction similar to the whole Falcon model at positive angles of attack over the entire range of Reynolds numbers.
- For extended surface scenarios, numerical results agreed well with experimental data, particularly at high Reynolds numbers.

In conclusion, the Falcon-inspired shapes proved highly effective in reducing drag, particularly in the subcritical Reynolds number range. The adaptability of these shapes suggests their potential in various aerodynamic applications, particularly in subcritical Reynolds number regions.

Acknowledgments

Use of AI tools declaration

The authors declare that they have not used Artificial Intelligence (AI) tools in the creation of this article.

Conflict of Interest

The authors declare that they have no known competing financial interests or personal relationships that could have appeared to influence the work reported in this paper.

References

[1] Sowoud KM, Al-Filfily AA, Abed BH (2020) Numerical Investigation of 2D Turbulent Flow past a Circular Cylinder at Lower Subcritical Reynolds Number. *IOP Conf Ser Mater Sci Eng* 881: 012160. https://doi.org/10.1088/1757-899X/881/1/012160

[2] Schlichting H, Gersten K (2016) Boundary-Layer Theory. *Springer* 1–799.

[3] Eun LC, Rafie ASM, Wiriadidjaja S, et al. (2018) An overview of passive and active drag reduction methods for bluff body of road vehicles. *Int J Eng Technol* 7: 53–56. https://doi.org/10.14419/ijet.v7i4.13.21328

[4] Frolov VA, Kozlova AS (2018) Influence of flat plate in front of circular cylinder on drag. *AIP Conf Proc* 2027: 1–9. https://doi.org/10.1063/1.5065182

[5] García-Baena C, Jiménez-González JI, Martínez-Bazán C (2021) Drag reduction of a blunt body through reconfiguration of rear flexible plates. *Phys Fluids* 33: 1–14. https://doi.org/10.1063/5.0046437

[6] Igarashi T (1981) Characteristics of the Flow around Two Circular Cylinders Arranged in Tandem : 1st Report. *Bull JSME* 24: 323–331. https://doi.org/10.1299/jsme1958.24.323

[7] Zdravkovich MM (1990) Conceptual overview of laminar and turbulent flows past smooth and rough circular cylinders. *J Wind Eng Ind Aerodyn* 33: 53–62. https://doi.org/10.1016/0167-6105(90)90020-D

[8] Xu G, Zhou Y (2004) Strouhal numbers in the wake of two inline cylinders. *Exp Fluids* 37: 248–56. https://doi.org/10.1007/s00348-004-0808-0

[9] Wu J, Welch LW, Welsh MC, et al. (1994) Spanwise wake structures of a circular cylinder and two circular cylinders in tandem. *Exp Therm Fluid Sci* 9: 299–308. https://doi.org/10.1016/0894-1777(94)90032-9

[10] Lin JC, Yang Y, Rockwell D (2002) Flow past two cylinders in tandem: instantaneous and averaged flow structure. *J Fluids Struct* 16: 1059–71. https://doi.org/10.1006/jfls.2002.0469

[11] Carmo BS, Meneghini JR, Sherwin SJ (2010) Secondary instabilities in the flow around two circular cylinders in tandem. *J Fluid Mech* 644: 395–431. https://doi.org/10.1017/S0022112009992473

[12] Lesage F, Gartshore IS (1987) A method of reducing drag and fluctuating side force on bluff bodies. *J Wind Eng Ind Aerodyn* 25: 229–45. https://doi.org/10.1016/0167-6105(87)90019-5

[13] Alam MM, Zhou Y (2008) Strouhal numbers, forces and flow structures around two tandem cylinders of different diameters. *J Fluids Struct* 24: 505–26. https://doi.org/10.1016/j.jfluidstructs.2007.10.001

[14] Zhao M, Cheng L, Teng B, et al. (2007) Hydrodynamic forces on dual cylinders of different diameters in steady currents. *J Fluids Struct* 23: 59–83. https://doi.org/10.1016/j.jfluidstructs.2006.07.003

[15] Wang L, Alam MM, Zhou Y (2018) Two tandem cylinders of different diameters in cross-flow: effect of an upstream cylinder on wake dynamics. *J Fluid Mech* 836: 5–42. https://doi.org/10.1017/jfm.2017.735

[16] Prasad A, Williamson CHK (1997) A method for the reduction of bluff body drag. *J Wind Eng Ind Aerodyn* 69-71: 155–167. https://doi.org/10.1016/S0167-6105(97)00151-7

[17] Han X, Wang J, Zhou B, et al. (2019) Numerical Simulation of Flow Control around a Circular Cylinder by Installing a Wedge-Shaped Device Upstream. *J Mar Sci Eng* 7: 422. https://doi.org/10.3390/jmse7120422

[18] Law YZ, Jaiman RK (2017) Wake stabilization mechanism of low-drag suppression devices for vortex-induced vibration. *J Fluids Struct* 70: 428–449. https://doi.org/10.1016/j.jfluidstructs.2017.02.005

[19] Alam MM, Sakamoto H, Zhou Y (2006) Effect of a T-shaped plate on reduction in fluid forces on two tandem cylinders in a cross-flow. *J Wind Eng Ind Aerodyn* 94: 525–551. https://doi.org/10.1016/j.jweia.2006.01.018

[20] Bearman PW, Harvey JK (1993) Control of circular cylinder flow by the use of dimples. *AIAA J* 31: 1753–6. https://doi.org/10.2514/3.11844

[21] Shih WCL, Wang C, Coles D, et al. (1993) Experiments on flow past rough circular cylinders at large Reynolds numbers. *J Wind Eng Ind Aerodyn* 49: 351–368. https://doi.org/10.1016/0167-6105(93)90030-R

[22] Yan F, Yang H, Wang L (2021) Study of the Drag Reduction Characteristics of Circular Cylinder with Dimpled Surface. *Water* 13: 197. https://doi.org/10.3390/w13020197

[23] Yokoi Y, Igarashi T, Hirao K (2011) The Study about Drag Reduction of a Circular Cylinder with Grooves. *J Fluid Sci Technol* 6: 637–650. https://doi.org/10.1299/jfst.6.637

[24] Haque MA, Rauf MA, Ahmed DH (2017) Investigation of Drag Coefficient at Subcritical and Critical Reynolds Number Region for Circular Cylinder with Helical Grooves. *Int J Marit Technol* 8: 25–33. https://doi.org/10.29252/ijmt.8.25

[25] Haidary FM, Mazumder A, Hasan MR, et al. (2020) Investigation for the drag reduction by introducing a passage through a circular cylinder. *Ann Eng* 1: 1–13.

[26] Asif MA, Gupta AD, Rana MJ, et al. (2016) Investigation of drag reduction through a flapping mechanism on circular cylinder. *AIP Conf Proc* 1754: 1–5. https://doi.org/10.1063/1.4958374

[27] Gehrke A, Richeux J, Uksul E, et al. (2022) Aeroelastic characterisation of a bio-inspired flapping membrane wing. *Bioinspir Biomim* 17: 065004. https://doi.org/10.1088/1748-3190/ac8632

[28] Buoso S, Dickinson BT, Palacios R (2017) Bat-inspired integrally actuated membrane wings with leading-edge sensing. *Bioinspir Biomim* 13: 016013. https://doi.org/10.1088/1748-3190/aa9a7b

[29] Shoshe MAMS, Islam A, Ahmed DH (2021) Effect of an upstream extended surface on reduction of total drag for finite cylinders in turbulent flow. *Int J Fluid Mech Res* 48: 27–44. https://doi.org/10.1615/InterJFluidMechRes.2021038255

[30] Islam A, Shoshe MAMS, Ahmed DH (2023) Reduction of Total Drag for Finite Cylinders in Turbulent Flow with a Half-C Shape Upstream Body. *Int J Fluid Mech Res* 50: 41–53. https://doi.org/10.1615/InterJFluidMechRes.2022045488

[31] Ghosh A, Gupta P, Jayant, et al. (2021) Metaheuristic optimization framework for drag reduction using bioinspired surface riblets. *ArXiv* 2: 1–7. https://doi.org/10.48550/arXiv.2109.09650

[32] Siddiqui NA, Agelin-Chaab M (2021) Nature-inspired solutions to bluff body aerodynamic problems: A review. *J Mech Eng Sci* 15: 1–52. https://doi.org/10.15282/jmes.15.2.2021.13.0638

[33] Cheney JA, Stevenson JPJ, Durston NE, et al. (2021) Raptor wing morphing with flight speed. *J R Soc Interface* 18: 1–14. https://doi.org/10.1098/rsif.2021.0349

[34] Sigrest P, Wu N, Inman DJ (2023) Energy considerations and flow fields over whiffling-inspired wings. *Bioinspir Biomim* 18: 046007. https://doi.org/10.1088/1748-3190/acd28f

[35] Bhardwaj H, Cai X, Win LST, et al. (2023) Nature-inspired in-flight foldable rotorcraft. *Bioinspir Biomim* 18: 46012. https://doi.org/10.1088/1748-3190/acd739

[36] Selim O, Gowree ER, Lagemann C, et al. (2021) Peregrine Falcon's Dive: Pullout Maneuver and Flight Control Through Wing Morphing. *AIAA J* 59: 3979–87. https://doi.org/10.2514/1.J060052

[37] Ponitz B, Schmitz A, Fischer D, et al. (2014) Diving-flight aerodynamics of a peregrine falcon (Falco peregrinus). *PLoS One* 9: e86506. https://doi.org/10.1371/journal.pone.0086506

[38] Pérez MG, Vakkilainen E (2019) A comparison of turbulence models and two and three dimensional meshes for unsteady CFD ash deposition tools. *Fuel* 237: 806–811. https://doi.org/10.1016/j.fuel.2018.10.066

[39] Nazari S, Zamani M, Moshizi SA (2018) Comparison between two-dimensional and three-dimensional computational fluid dynamics techniques for two straight-bladed vertical-axis wind turbines in inline arrangement. *Wind Eng* 42: 47–64. https://doi.org/10.1177/0309524X18780384

[40] Stringer RM, Zang J, Hillis AJ (2014) Unsteady RANS computations of flow around a circular cylinder for a wide range of Reynolds numbers. *Ocean Eng* 87: 1–9. https://doi.org/10.1016/j.oceaneng.2014.04.017

[41] Rafi AH, Haque MR, Ahmed DH (2022) Two-dimensional analogies to the deformation characteristics of a falling droplet and its collision. *Archive Mech Eng* 69: 21–43. https://doi.org/10.24425/ame.2021.139649

[42] Anderson JD (2011) *Fundamentals of Aerodynamics* (New York: McGraw-Hill Education).

[43] Johansson C, Linder ET, Hardin P, et al. (1998) Bill and body size in the peregrine falcon, north versus south: Is size adaptive? *J Biogeogr* 25: 265–273. https://doi.org/10.1046/j.1365-2699.1998.252191.x

[44] Holman JP (2011) *Experimental Methods for Engineers* (New York: McGraw-Hill), 60–165.

[45] Menter FR, Langtry RB, Likki SR, et al. (2006) A correlation-based transition model using local variables - Part I: Model formulation. *J Turbomach* 128: 413–422. https://doi.org/10.1115/1.2184352

[46] Malan P, Suluksna K, Juntasaro E (2009) Calibrating the γ-Reθ transition model for commercial CFD. *47th AIAA Aerospace Sciences Meeting including the New Horizons Forum and Aerospace Exposition* (Orlando). https://doi.org/10.2514/6.2009-1142

[47] Menter FR (1993) Improved Two-Equation κ-ω Turbulence Models for Aerodynamic Flows. *NASA TM* 103975. https://doi.org/10.2514/6.1993-2906

[48] Munson BR, Young DF, Okiishi TH (1998) *Fundamentals of fluid mechanics* (Wiley).

[49] Rosetti GF, Vaz G, Fujarra ALC (2012) URANS calculations for smooth circular cylinder flow in a wide range of reynolds numbers: Solution verification and validation. *J Fluids Eng Trans ASME* 134: 121103. https://doi.org/10.1115/1.4007571

[50] Yuce MI, Kareem DA (2016) A numerical analysis of fluid flow around circular and square cylinders. *J Am Water Works Assoc* 108: 546–554. https://doi.org/10.5942/jawwa.2016.108.0141

[51] Hoener SF (1965) Pressure Drag *Fluid Dynsmic Drag* (New York, United States: Hoener Fluid Dynamics), 5–8.

[52] Achenbach E (1971) Influence of surface roughness on the cross-flow around a circular cylinder. *J Fluid Mech* 46: 321–335. https://doi.org/10.1017/S0022112071000569

[53] Hojo T (2015) Control of flow around a circular cylinder using a patterned surface. *WIT Transactions on Modelling and Simulation* 12: 245–256. https://doi.org/10.2495/CMEM150221

[54] Selig MS (2003) Low Reynolds Number Airfoil Design Lecture Notes, 1–43.

[55] Sohankar A, Khodadadi M, Rangraz E, et al. (2019) Control of flow and heat transfer over two inline square cylinders. *Phys Fluids* 31: 123604. https://doi.org/10.1063/1.5128751

[56] Aguedal L, Semmar D, Berrouk AS, et al. (2018) 3D vortex structure investigation using Large Eddy Simulation of flow around a rotary oscillating circular cylinder. *Eur J Mech B/Fluids* 71: 113–125. https://doi.org/10.1016/j.euromechflu.2018.04.001

[57] Ji L, Du H, Yang LJ, et al. (2023) Research on the drag reduction characteristics and mechanism of a cylinder covered with porous media. *AIP Adv* 13: 035220. https://doi.org/10.1063/5.0141832

[58] Qi J, Qi Y, Chen Q, et al. (2022) A study of drag reduction on cylinders with different v-groove depths on the surface. *Water* 14: 36. https://doi.org/10.3390/w14010036